Journal of Orthopaedic Translation 48 (2024) 25–38

Contents lists available at ScienceDirect

Journal of Orthopaedic Translation

journal homepage: www.journals.elsevier.com/journal-of-orthopaedic-translation

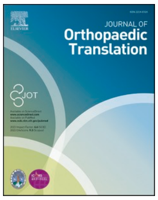

Original Article

A 3D-printed scaffold composed of Alg/HA/SIS for the treatment of diabetic bone defects

Jie Tan [a,b,c,1], Zecai Chen [a,1], Zhen Xu [a], Yafang Huang [a,c], Lei Qin [a], Yufeng Long [a], Jiayi Wu [a], Wanrong Luo [a], Xuchao Liu [a], Weihong Yi [a,***], Huaiyu Wang [b,**], Dazhi Yang [a,*]

[a] Department of Spine Surgery & Innovative Laboratory of Orthopedics, Huazhong University of Science and Technology Union Shenzhen Hospital, Shenzhen, Guangdong, 518052, China
[b] Center for Human Tissues and Organs Degeneration, Shenzhen Institutes of Advanced Technology, Chinese Academy of Sciences, Shenzhen, 518055, China
[c] Orthopaedic Department, Wuhan Fourth Hospital, Wuhan, 430030, China

ARTICLE INFO

Keywords:
Angiogenesis
Diabetic bone healing
Immunomodulation
Osteogenesis small intestinal submucosa

ABSTRACT

Background: Diabetic bone healing remains a great challenge due to its pathological features including biochemical disturbance, excessive inflammation, and reduced blood vessel formation. In previous studies, small intestine submucosa (SIS) has been demonstrated for its immunomodulatory and angiogenic properties, which are necessary to diabetic bone healing. However, the noticeable drawbacks of SIS such as fast degradation rate, slow gelling time, and weak mechanical property seriously impede the 3D printing of SIS for bone repair.

Method: In this study, we developed a novel kind of 3D-printed scaffold composed of alginate, nano-hydroxyapatite, and SIS. The morphological characterization, biocompatibility, and *in vitro* biological effects of the scaffolds were evaluated, and an established diabetic rat model was used for testing the *in vivo* biological effect of the scaffold after implantation.

Results: The *in vitro* and *in vivo* results show that the addition of SIS can tune the immunomodulatory properties and angiogenic and osteogenic performances of 3D-printed scaffold, where the macrophages polarization of M2 phenotype, migration and tube formation of HUVECs, as well as osteogenic expression of ALP, are all improved, which bode well with the functional requirements for treating diabetic bone nonunion. Furthermore, the incorporation of alginate substantially improves the printability of composites with tunable degradation properties, thereby broadening the application prospect of SIS-based materials in the field of tissue engineering.

Conclusion: The fabricated 3D-printed Alg/HA/SIS scaffold provides desirable immunomodulatory effect, as well as good osteogenic and angiogenic performances *in vitro* and *in vivo*, which properties are well-suited with the requirement for treating diabetic bone defects.

Translational potential of this article: The incorporation of SIS and alginate acid not only provides good printability of the newly fabricated 3D-printed Alg/HA/SIS scaffold, but also improves its immunoregulatory and angiogenic properties, which suits well with the requirement for treating diabetic bone disease and opens up new horizons for the development of implants associating diabetic bone healings.

1. Introduction

Critical-size bone defects are a serious kind of bone diseases caused by many disorders such as trauma, tumors and osteoporosis [1–4]. When critical-size bone defects occur, self-healing is a mission impossible without the aid of implants. Recently, the emergence and rapid

---

* Corresponding author. Department of Spine Surgery & Innovative Laboratory of Orthopedics, Huazhong University of Science and Technology Union Shenzhen Hospital, Shenzhen, Guangdong, 518052, China.

** Corresponding author. Center for Human Tissues and Organs Degeneration, Shenzhen Institutes of Advanced Technology, Chinese Academy of Sciences, Shenzhen, 518055, China.

*** Corresponding author. Department of Spine Surgery & Innovative Laboratory of Orthopedics, Huazhong University of Science and Technology Union Hospital, Guangdong, 518052, China.

E-mail addresses: szyiwh@163.com (W. Yi), hy.wang1@siat.ac.cn (H. Wang), qpopop1977@163.com (D. Yang).

[1] These authors have contributed equally to this work

https://doi.org/10.1016/j.jot.2024.07.006
Received 3 June 2024; Received in revised form 9 July 2024; Accepted 11 July 2024

development of 3D printing open up new horizons for the development of implants associating bone healing [5–8]. Taking advantage of 3D printing technique, bone implants can be fabricated with different shapes, sizes, and pore structures to match the specific requirements of damaged bone repair [6]. Nevertheless, there are still great challenges for damaged bone repair using implants, especially in some pathological conditions such as diabetes [9,10]. As reported, the bone healing of patients with diabetes mellitus is more difficult than that under normal conditions. This is because the pathological circumstance of diabetes mellitus is very complicated, where biochemical disturbance, excessive inflammation, and high expression of reactive oxide species are all involved [10–14]. The microenvironment of bone marrow is also changed, which hampers the formation of new bones containing small blood vessels [14,15]. Therefore, the bone healing under diabetes conditions is difficult, and hence the implanted biomaterials designed with special functions are urgently needed.

As is well known, osteogenic capacity is the primary function of implanted biomaterials for treating bone defects [6,16–18]. Nowadays, various kinds of artificial biomaterials including metals, ceramics and synthetical polymers have been developed for bone implantation [6,19]. However, the biomedical metals such as Ti alloy and synthetical polymers such as poly-ether-ether-ketone are inherently bio-inert, of which the osteogenic performances are not good enough [20]. Alternatively, biomedical ceramics such as hydroxyapatite are outstanding for their pro-osteogenic function [21,22]. However, the mechanical mismatching between ceramics and natural bones is a knotty problem when the long-standing implants should bear forces in human bodies. What's more, in addition to osteogenesis, the other biological functions such as immunomodulation and angiogenesis should be taken into overall consideration during the sensitive and complicated process of bone regeneration post-implantation [23,24].

Small intestine submucosa (SIS) is a kind of extracellular matrix derived from decellularization of small intestine, whereby the majority of bioactive extracellular matrix (ECM) can be maintained [25]. A series of studies have shown that the SIS-based materials are a promising kind of bioactive materials, which can facilitate the regeneration of tissues such as urinary bladder, skin, uterus, abdominal wall, and bone [26–30]. Recently, we have demonstrated that there are multiple bioactive compounds in SIS, which can induce the polarization of macrophages into M2 phenotype, creating a favorable immune microenvironment for the subsequent healing process [28,31]. Moreover, SIS also provides good angiogenic capacity as it can facilitate the proliferation, migration, and tube formation of human umbilical vein endothelial cells (HUVECs) *in vitro* [25]. However, there are still some noticeable drawbacks of SIS such as fast degradation rate, slow gelling time, and weak mechanical property, which limit its applications in biomedical fields.

Sodium alginate is a kind of natural polysaccharides derived from brown algae or sargassum, which is composed of β-D-mannuronic acid and α-L-guluronic acid [32–34]. The sodium alginate can readily react with calcium chloride to form calcium alginate and transform into a

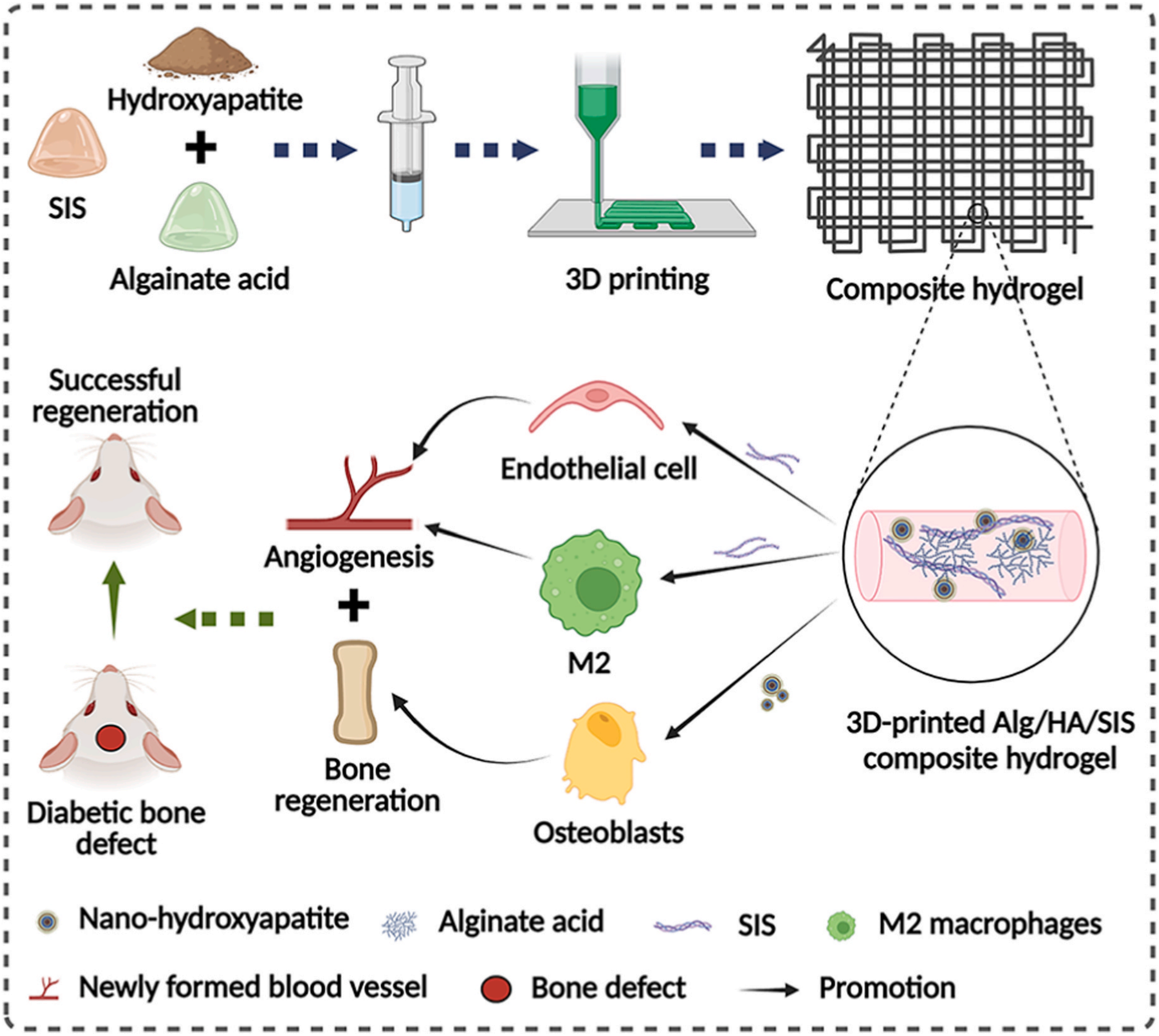

Fig. 1. The graphical abstract of this study.

hydrogel state [34]. Due to the easy-making procedure, the alginate-based scaffold has been widely used in tissue engineering [33–35]. However, its sole use can not meet the functional requirement of tissue regeneration (including bone regeneration) as the bioactive components are still lacking [16,36,37]. To this end, by combining the easily-shaped sodium alginate with ceramic (nano-hydroxyapatite) and SIS providing bioactivities, their functions and mechanical properties can be complementary to each other, and the composited biomaterial can be fabricated into personalized implants by 3D printing. As demonstrated in our study, this kind of composition exhibits good performances *in vitro* and *in vivo* with respect to the printability, immunomodulatory property, as well as the angiogenesis and osteogenesis (Fig. 1), whose functions match suitably well with the requirement for repairing bone defects under diabetic pathological condition.

2. Materials and methods

2.1. Fabrication of 3D Alg/HA/SIS composited scaffold

SIS sheets were prepared and lyophilized according to our previous study. The lyophilized SIS sheets were then sliced, grounded, and digested with pepsin (Sigma, USA) to prepare SIS stock solution with its final concentration to be 1 %. The alginate stock solution was prepared by fully dissolving 0.8 g sodium alginate in 10 mL deionized water to reach a concentration of 8 %. Meanwhile, part of the sodium alginate stock solution was added with 2 % nano-hydroxyapatite particles. Afterward, the SIS stock solution and sodium alginate solution with or without nano-hydroxyapatite were mixed in a ratio of 1:1 to prepare composited scaffolds. All the scaffolds were printed using a 3D-printing machine (Regenovo, China), with 3D grid pattern being designed. The parameters for printing were set as below: nozzle of 27G, printing speed of 44 mm/s, pneumatic pressure of 0.046 MPa, receiver plate temperature of −20 °C. Finally, the fabricated 3D scaffolds were immersed in 5 % $CaCl_2$ for crosslinking.

2.2. Morphological, chemical, and mechanical properties

After sample preparation, light microscope and scanning electron microscope (SEM) were used to observe the morphological characters of those 3D-printed scaffolds. Prior to SEM observation, the samples were lyophilized and sputtered with gold, and then examined by the EVO 10 SEM apparatus (ZEISS, Germany) with an accelerating voltage of 20.0 kV. The different composites were determined for their fourier transform infrared spectroscopy (FTIR) spectra using FTIR spectrometer (Thermo Scientific, USA) after being mixed and grinded with KBr. The surface element distribution of those 3D-printed scaffolds was measured by energy dispersive spectroscopy (EDS, ZEISS, Germany). The mechanical behaviors of those 3D-printed scaffolds were tested by a mechanical testing instrument (CARE, China), where the compressive properties of those scaffolds (diameter: 10 mm; height: 10 mm) were tested at a speed of 1 mm/min, and the stress–strain curves were calculated and analyzed according to the load and displacement parameters.

2.3. Swelling and degradation behaviors

The swelling test was performed as follows: the lyophilized 3D-printed scaffolds were immersed in 1.0 × PBS (pH = 7.4) solution, and then put into 37 °C condition to reach equilibrium. At predetermined time points, the samples were taken out to remove excess water on the surface and weight. The swelling ratio was calculated according to the following equation:

$$\text{Swelling ratio (\%)} = W_t/W_0 \times 100\%$$

Where W_0 was the initial weight of the scaffolds, and W_t was the weight of scaffolds at predetermined time points.

After reaching equilibrium in 1.0 × PBS solution, $5 \times 10 \times 10\ mm^3$ of each 3D-printed scaffold was weighed, and then agitated in a thermostatic shaker at 37 °C with a rotatory speed of 50 r/min. At the predetermined time points, residual masses were weighed and recorded, and the degradation ratio was calculated according to the following equation:

$$\text{Degradation ratio (\%)} = M_t/M_0 \times 100\%$$

Where M_0 was the initial mass of the scaffolds, and M_t was the mass of scaffolds at predetermined time points.

2.4. In vitro biocompatibility

Bone marrow mesenchymal stem cells (BMSCs) were seeded onto the 3D-printed scaffolds at a density of 2×10^3 cells per sample when using 96-well plates as the holders. Dulbecco's modified Eagle's medium (DMEM, HyClone) supplemented with 10 % fetal bovine serum (FBS, Gibco) was used as the culture medium and refreshed every other day. Cell proliferation was tested by a CCK-8 kit (Dojindo, Japan) at day 1, 2, 3, and 5 according to the manufacturer's protocols. After adding CCK-8 reagent and incubating for another 2 h at 37 °C, the medium of each group was measured by a microplate reader (Thermo Scientific, USA) at a wavelength of 450 nm.

Live/dead assay was also performed to evaluate the cytotoxicity of different scaffolds. After culturing with DMEM for 2 days, the cells were stained with Calcein-AM and propidium iodide (PI) (Beyotime, China) following the manufacture's protocols, and the live/dead cells were visualized under a confocal laser scanning microscope (CLSM, Nikon, Japan).

2.5. In vitro responses of macrophages

Raw264.7 cells were seeded onto the 3D-printed scaffolds at a density of 2×10^3 cells per sample when using 96-well plates as the holders. Dulbecco's modified Eagle's medium (DMEM, HyClone) supplemented with inactivated 10 % fetal bovine serum (FBS, Gibco) was used as the culture medium and refreshed every other day. After culturing for 2 days, the cells on samples were fixed by 4 % paraformaldehyde, permeabilized with 0.1 % Triton-X 100, and blocked by 10 % goat serum. Subsequently, the cells were co-incubated with primary antibodies of mannose receptor (CD206) (1:200 dilution, ab300621, Abcam), inducible nitric oxide synthase (iNOS) (1:200 dilution, ab178945, Abcam), and F4/80 (1:200 dilution, ab6640, Abcam) at 4 °C overnight, respectively. Alexa Fluor 594 goat anti-rat (1:1000 diluted, ab150077, Abcam) and Alexa Fluor 488 goat anti-rabbit secondary antibodies (1:1000 diluted, ab150077, Abcam) were utilized for another 1 h of incubation at room temperature. Finally, the cells in different groups were counterstained with DAPI and then sealed with anti-fluorescent quenching coverslips. The immunofluorescence of cells was observed under a confocal laser scanning microscope (CLSM, Nikon, Japan) and analyzed using ImageJ 1.8.0 software.

2.6. In vitro angiogenesis

2.6.1. Scratch assay

Human Umbilical Vein Endothelial Cells (HUVECs) were seeded into a 6-well plate at a density of 1.2×10^6 per well and cultured with DMEM medium at an absence of fetal bovine serum (FBS) for 24 h. A scratch was made by a 200 μL tip and the unattached cells were rinsed using PBS solution. Afterwards, extracts from those 3D-printed scaffolds were prepared according to ISO 10993-12: 2021 and added for co-culture. After 0, 24, and 48 h of incubation, images were taken using a light microscope and analyzed by ImageJ 1.8.0. The migration rate was calculated according to the following equation:

$$\text{Migration rate (\%)} = (S_0\text{-}S_t)/S_0 \times 100\%$$

Where S_0 was the primary area of scratches and S_t was the area of scratches at predetermined time points.

2.6.2. Tube formation assay

50 μL Matrigel (Sigma, USA) was added to each well of a 48-well plate on ice, and then transferred to 37 °C for gelation. Subsequently, 2.0×10^4 HUVECs before P6 were seeded into each well, and co-cultured with extracts as mentioned above. After culturing for 0, 2, and 8 h, tube formation in each group were observed using a light microscope. ImageJ 1.8.0 software was used to analyze the number of branches, junctions, and nodes, as well as total length of tubes in each group.

2.7. In vitro osteogenesis study

MC3T3-E1 cells were seeded onto the 3D-printed scaffolds at a density of 1.0×10^5 per sample when using 26-well plates as the holders. Dulbecco's modified Eagle's medium (DMEM, HyClone) supplemented with 10 % fetal bovine serum (FBS, Gibco) was used as the culture medium, mixed 1:1 with the extracts of the scaffold, and refreshed the culture medium every other day. After culturing for 14 days, the cells in different groups were fixed by 4 % paraformaldehyde solution and then subjected to alkaline phosphatase (ALP) staining (Beyotime, China). The stained cells were observed under a light microscope and analyzed by ImageJ 1.8.0.

2.8. Establishment of diabetic animal model and surgical procedures

All animal studies were approved by the institutional animal care and use committee (IACUC) of Shenzhen TopBiotech Co., Ltd. (IACUC No.2023-0302), and the procedures were complied with the Principles of Laboratory Animal Care released by the National Society for Medical Research. Sprague Dawley (SD) rats weighed 200 g were intraperitoneally injected with 75 mg/kg streptozotocin (MCE, USA) after fasting for 24 h. Blood sugar was monitored after 3 days, and another dose of 20 mg/kg streptozotocin was supplemented if their blood sugar level was lower than 11.1 mmol/L, to make sure the successful establishment of diabetic animal model. 2 weeks later, those SD rats were anesthetized with isoflurane by mask inhalation. After skin preparation and disinfection, a 1.5 cm midsagittal incision was performed to expose the rat skull, then a 5 mm dental trephine bur was used to create critical-sized bone defect. The incisions were closed after implantation of different 3D-printed scaffolds. Meanwhile, the scaffolds were subcutaneously implanted into the back of diabetic rats to explore their effects on immune response and angiogenesis. After operation, one dose of 30 mg/kg ampicillin and 2 mg/kg meloxicam were prescribed for preventing infection and relieving pain.

2.9. Micro-CT scan

After 4 and 8 weeks post-operation, the skulls of experimental rats were harvested and scanned by a micro-CT (NEMO, China) with a voltage of 80 kV, current of 100 μA, and voxel size of 18 μm. 3D images were constructed with its attached micro-CT reconstruction software with a grayscale set at 220. The regenerated volume of new bone, bone volume fraction (BV/TV), and bone mineral density (BMD) were calculated and analyzed, respectively.

2.10. Hematoxylin-Eosin and Masson's trichrome staining

After micro-CT scanning, the harvested samples were fixed by 4 % paraformaldehyde and decalcified with 10 % ethylene diamine tetracetic acid (EDTA) (Solarbio, China) in a shaker at 37 °C for 1 month. The EDTA solution was refreshed once a week. After being fully decalcified, the specimens were dehydrated by graded alcohol, embedded in paraffin, and sliced by a rotary microtome (Leica, German) with a thickness of 5 μm. Hematoxylin-Eosin (HE) and Masson's trichrome staining (Beyotime, China) was conducted, respectively. The newly formed bone and blood vessels were observed and analyzed based on the obtained photographs.

2.11. Immunohistochemistry and immunofluorescence analyses

Paraffin-embedded slices of rat skins and skulls containing different samples were dewaxed, rehydrated, and then water-bathed in sodium citrate solution (ZSGB-BIO, China) (pH = 6.2) for antigen retrieval (60 °C, overnight). Subsequently, the slices were treated with 3 % H_2O_2 to inactivate hydrogen peroxidases, and 10 % goat serum solution was used to block non-specific antigens. The treated slices were incubated with CD206 (1:500 dilution, ab300621, Abcam), CD31 (1:500 dilution, ab281583, Abcam) and ALP (1:500 dilution, ab300621, Abcam) primary antibodies respectively, and then incubated with their corresponding secondary antibodies. Photographs were captured using a fluorescent microscope and light microscope, and their expression changes were analyzed by ImageJ 1.8.0.

2.12. Statistical analysis

SPSS of version 22.0 (IBM, Chicago, USA) software package was exploited to analyze the expression changes in this research. Variables were presented as mean ± standard deviation. One-way analysis of variance (ANOVA) followed with *post hoc* Tukey's test was applied to compare the parameters between different groups, and $p < 0.05$ was considered statistically significant.

3. Results and discussion

3.1. Characterization of the 3D printed scaffolds

In the present study, alginate acid, nano-hydroxyapatite and SIS were utilized as the basic materials to construct 3D-printed scaffolds. As shown in Fig. 2A, all the Alg, Alg/HA, and Alg/HA/SIS scaffolds were successfully fabricated, where the Alg/HA and Alg/HA/SIS groups exhibited a slightly yellow hue, and the opaque character of Alg/HA and Alg/HA/SIS might be ascribed to the presence of nano-hydroxyapatite. The scanning electron microscopy (SEM) results indicated that the addition of SIS smoothened the surface of the 3D-printed scaffold in the Alg/HA/SIS group, while the surfaces of the Alg and Alg/HA groups were relatively rough (Fig. 2B). Furthermore, the EDS scans revealed that the Alg/HA/SIS group had a higher fraction of calcium elements, with calcium ratios of 13.8 %, 13.8 %, and 14.6 % in the Alg, Alg/HA, and Alg/HA/SIS groups, respectively (Fig. 2C). These findings suggest that the addition of SIS played a more beneficial role in integrating calcium into the Alg/HA/SIS group, which might partially explain the increased regeneration of new bones in diabetic rats in this group presented at later sections. The mechanical tests revealed that the stress–strain curves were: Alg > Alg/HA/SIS > Alg/HA, the highest compressive stress of 36.4 MPa was detected in the Alg group, while the Alg/HA and Alg/HA/SIS were 18.5 and 32.6 MPa, respectively (Fig. S1). Therefore, the addition of hydroxyapatite and SIS had to some extent reduced the mechanical performance of the Alg-based scaffold. While no distinct functional groups were detected among groups by FTIR (Fig. S2).

3.2. Swelling and degradation behavior

As shown in Fig. 3A, the swelling ratio of Alg/HA/SIS scaffold was higher than that of Alg and Alg/HA scaffolds during the initial 0.5 h, which suggested that the incorporation of SIS could facilitate water

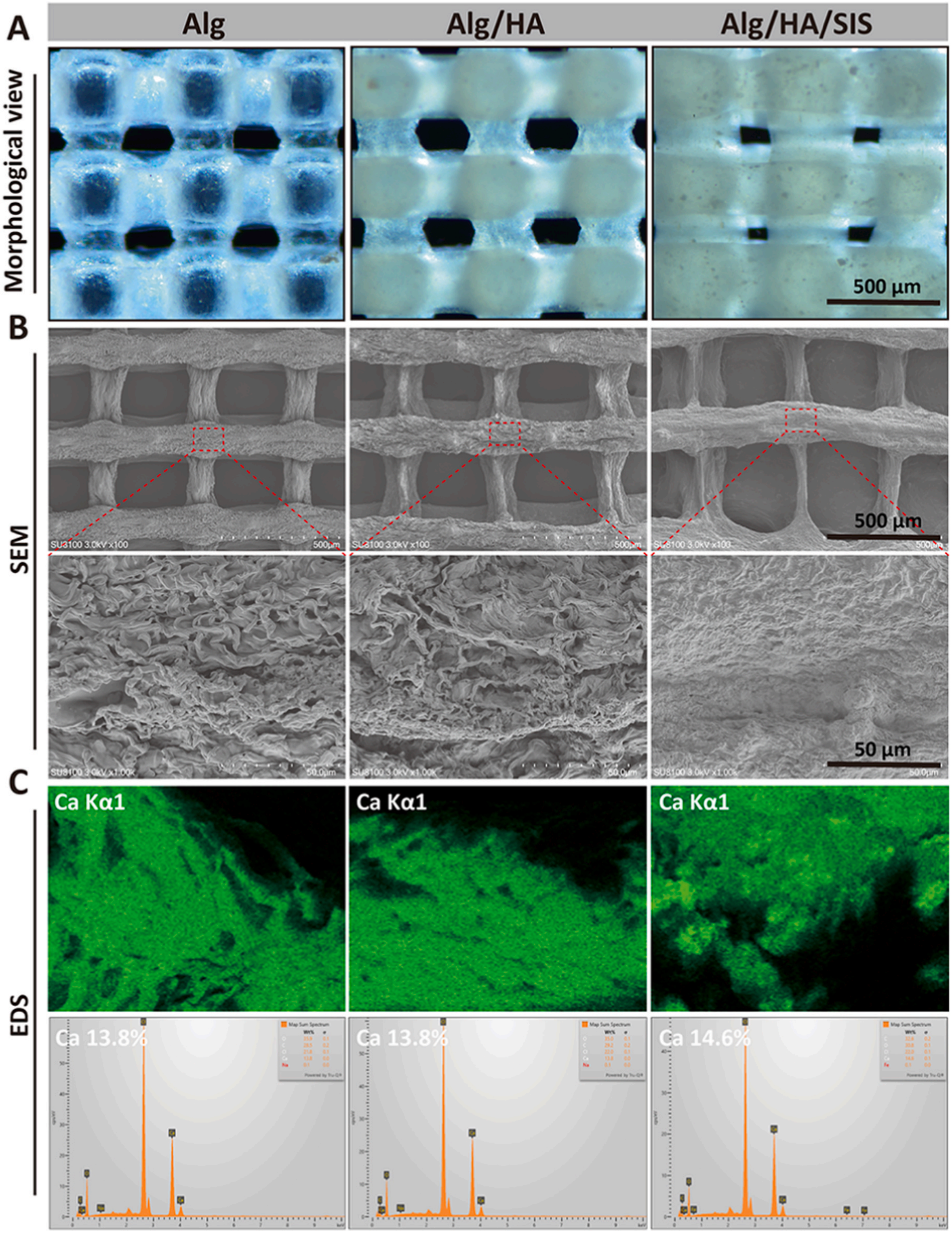

Fig. 2. The characterizations of different 3D-printed scaffolds. (A) Morphological view; (B) SEM observation; (C) EDS analysis.

absorption (Fig. 3A). However, the addition of nano-hydroxyapatite appeared to decrease the swelling behavior of the 3D-printed scaffolds, as the Alg/HA group exhibited lower water absorbance than the Alg group at all time points. Degradation assay demonstrated that the Alg/HA/SIS exhibited significantly faster degradation performance than the other two groups (Fig. 3B). It is noteworthy that pure SIS can not transform into a hydrogel state at the concentration of 1 %, a concentration that we used for 3D printing in this study. In our prior study, the lowest concentration of SIS needed to form a hydrogel scaffold in 37 °C condition should be at least higher than 2 %, while the gelling behavior was also varied by storage intervals of the harvested SIS sheets [31,38]. Interestingly, the degradation curve of the Alg/HA scaffold was slightly slower than that of the Alg scaffold, although differences between those two groups were not statistically significant, which suggested that the addition of nano-hydroxyapatite particles could partially reinforce the stability of the 3D-printed scaffold.

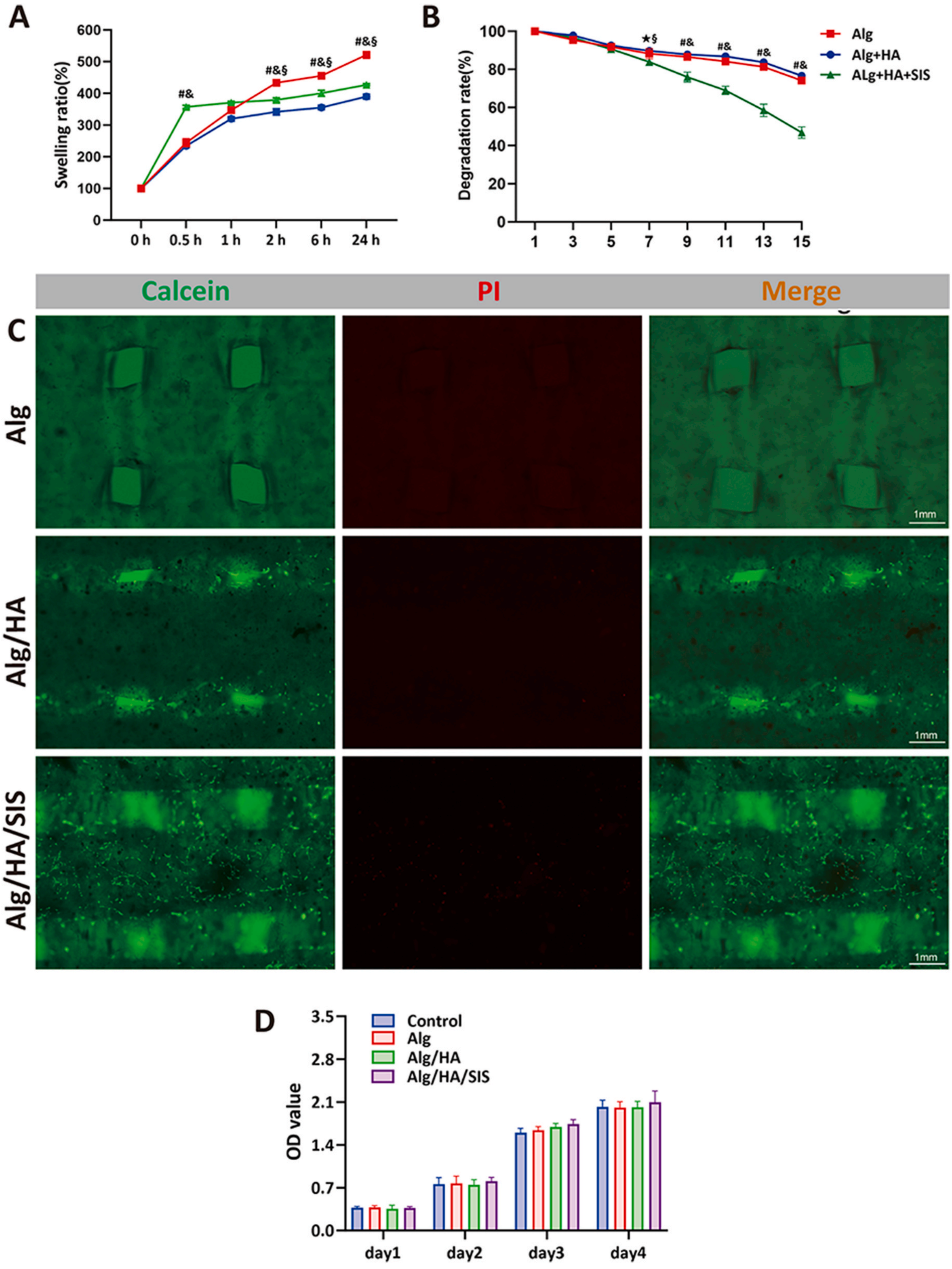

Fig. 3. The cytocompatibility of different 3D-printed scaffolds. (A) Swelling ratio; (B) Degradation rate; (C) Calcein/PI staining; (D) CCK-8 assay.

3.3. Biocompatibility of the 3D printed scaffolds

The biocompatibility of the 3D-printed composite scaffold was assessed by live/dead and CCK-8 assay. As shown in Fig. 3C, most of the cells adhered on different scaffolds were viable by fluorescing green, where the highest number of attached cells was observed in the Alg/HA/SIS group, which suggested that the existence of bioactive compounds, such as collagens, polysaccharides, cytokines, and exosomes in SIS, might significantly contribute to the increased cell adhesion in the Alg/HA/SIS group [26,28,30]. However, those bioactive components were absent in alginate acid and synthetical materials, while some degradations of synthetic materials might even be toxic. For instance, Donate and coworkers reported that the degradation of PLA can lower the pH value to 5.07, a pH that could seriously interrupt the physiological regenerative process, while the addition of $CaCO_3$ particles maintained the implanted area at a pH of 7.6 [39]. Therefore, the incorporation of SIS confers the 3D-printed scaffold comparable advantage with relation to the biocompatibility and bioactivity in this study. Furthermore, the CCK-8 assay revealed that no statistically significant differences of proliferation were detected among the three groups (Fig. 3D), which indicated that the biocompatibility of those 3D-printed composite scaffolds was excellent. Those findings were consistent with previously published researches, which reported that the decellularized ECM such as SIS not only had good bioactivity but also had excellent biocompatibility [38,40].

3.4. Incorporation of SIS improves angiogenic behavior of the 3D-printed scaffold in vitro

Angiogenic behavior is a crucial indicator for evaluating the efficacy of 3D-printed materials in bone regeneration, especially in diabetic conditions [41,42]. To determine the angiogenic induction properties of the 3D-printed scaffolds, a tube formation assay was employed. Results of tube formation assay revealed that the addition of SIS significantly enhanced the angiogenic induction capacity of the Alg/HA/SIS scaffold in terms of the number of branches and total lengths (Fig. 4A–C-D). This finding was in line with our previous studies, which validated that VEGF and bFGF were gradually released from the decellularized SIS scaffold, where angiogenic gene expressions such as KDR, Notch1, and Ang2 of HUVECs were consequently elevated [30]. Interestingly, the angiogenic induction capacity in the Alg/HA group was found to be significantly stronger than the control and Alg groups in this study, where tiny elements released from nano-hydroxyapatite particles might be responsible for this observation [43]. Moreover, migration assay showed that the highest migration rate was detected in the Alg/HA/SIS group at all time points (Fig. 4B and E). Collectively, the experiments in this section revealed that the addition of SIS significantly increased the angiogenic induction and migration of vascular-related cells, which significantly contributed to the accelerated healing process of diabetic bone in the later study.

3.5. Enhanced M2 macrophage polarization was elicited by the addition of SIS

The innate immune response of implants is another key factor for regulating the healing process of bone defect [44,45]. As described above, macrophages are predisposed to polarize towards a M1 phenotype under diabetic conditions, where multiple inflammatory cytokines were released to hamper subsequent bone healing, while M2 macrophages are demonstrated to be conducive for diabetic bone healing [3]. Interestingly, SIS has been well proved for its immunomodulatory property for regeneration by inducing macrophages towards M2 phenotype to facilitate tissue regeneration [28]. However, it remains unclear whether this property of SIS scaffold is preserved in this newly fabricated 3D-printed composite scaffold. Therefore, Raw264.7 cells were used to study the immune response of those 3D-printed scaffolds, where the immunofluorescences of CD206/F4/80 and iNOS/F4/80 were stained, respectively. Accordingly, the expression of CD206 in the Alg/HA and Alg/HA/SIS groups were both significantly elevated (*vs.* control group, $p < 0.05$), where the highest number of positive cells was observed in the Alg/HA/SIS group (39.67 ± 3.95 %) among all the three groups (Fig. 5B–D). This suggested that the bioactivity of SIS was successfully preserved during 3D-printing, which was further supported by the FTIR analysis without the detection of new chemical functional bonds in the 3D-printed scaffolds (Fig. S2), those results indicated that the physicochemical properties of the incorporated materials were retained. Meanwhile, nano-hydroxyapatite particles had also been proved to promote the M2 polarization of macrophages to some extent [41], which study partially explicated why the Alg/HA group detected higher CD206 expression than the control group ($p < 0.05$). However, no different expression changes of iNOS were detected among the three groups of those 3D-printed scaffolds, signifying no inflammation of the 3D-printed scaffolds (Fig. 5A–E).

3.6. In vitro osteogenic performance of the 3D-printed scaffolds

In this study, direct osteogenic behavior of those 3D-printed scaffolds was also investigated. The ALP staining showed that all three 3D-printed groups exhibited stronger ALP staining than the control group, where the highest ALP expression was detected in the Alg/HA/SIS group (Fig. 5C–F). These findings were aligned with the EDS scan analyses aforementioned, which showed that the highest percentage of calcium element was detected in the Alg/HA/SIS group. Meanwhile, the incorporation of nano-hydroxyapatite particles had also displayed advantages in elevating alkaline phosphatase levels, where some articles had documented the significant role of nano-hydroxyapatite particles in accelerating bone injury healing [22,42]. Furthermore, the composition of nano-hydroxyapatite can be customized to meet various requirements, thereby broadening its potential applications in bone tissue engineering [35,43,46]. For instance, Cheng and coworkers discovered that the functionalization of nano-hydroxyapatite with Sr^{2+} significantly promoted osteogenesis and angiogenesis through a process of slow release [22].

3.7. Micro-CT scan analysis: the 3D-printed Alg/HA/SIS scaffold enhanced bone regeneration in diabetic rats

The osteogenic performance of the 3D-printed scaffolds was evaluated *in vivo*, where a diabetic bone defect model of Sprague–Dawley (SD) rats was established for implantation of the 3D-printed scaffolds. Micro-CT scans revealed that the highest bone regenerative volume and density were observed in the Alg/HA/SIS group both after 4 and 8 weeks post-implantation (Fig. 6A). As shown in Fig. 6B–D, the BV/TV ratio in the Alg/HA/SIS group was calculated as 7.71 ± 0.98 % and 18.82 ± 2.26 % after 4 and 8 weeks post-implantation, respectively ($p < 0.05$, *vs.* the control and Alg/HA groups). Bone mineral density (BMD) was also improved as well, where the BMD in the Alg/HA/SIS group was 0.94 ± 0.06 and 1.08 ± 0.03 g/cm^3 after 4 and 8 weeks of implantation ($p < 0.05$, *vs.* the control and Alg/HA groups). What's more, the regenerated bone volume in the Alg/HA/SIS group was 3.98 ± 0.39 and 6.55 ± 0.78 mm^3 after 4 and 8 weeks of implantation ($p < 0.05$, *vs.* the control and Alg/HA groups), respectively. Interestingly, the Alg/HA scaffold group also provided better osteogenic performance as compared to the control group, although the differences were not as pronounced as that of the Alg/HA/SIS group. These results indicated that the 3D-printed Alg/HA/SIS composite scaffold significantly accelerated the regenerative process of the diabetic bone defect *in vivo*, which was in line with our previous conclusions [28].

3.8. HE and Masson's trichrome staining: more regenerated bone volume was observed in the 3D-printed Alg/HA/SIS scaffold

HE and Masson' trichrome stainings were performed to further evaluate the regenerative effect of those 3D-printed scaffold from histological aspects. Similar with the results of micro-CT scans, the Alg/HA/SIS group provided the most pronounced effect of bone regeneration after 4 and 8 weeks of implantation (Figs. 6E and 7A–C). Correspondingly, as shown in Fig. 7B and C, the ratios of the newly formed bone/total bone (NB/TB) in the Alg/HA/SIS group were 52.52 ± 2.80 % after 4 weeks and 63.81 ± 2.98 % after 8 weeks ($p < 0.05$, *vs.* the control and Alg/HA groups), respectively. We further assessed the regenerative effects by analyzing the ratios of lamellar bone/total bone (LB/TB) in detail. The LB/TB ratios at 4 and 8 weeks were 26.11 ± 2.17 % and 38.12 ± 2.57 % ($p < 0.05$, *vs.* the control and Alg/HA groups), respectively. Interestingly, we also found the bone regenerative effect in the Alg/HA group was higher than that of the Alg group ($p < 0.05$, *vs.* the

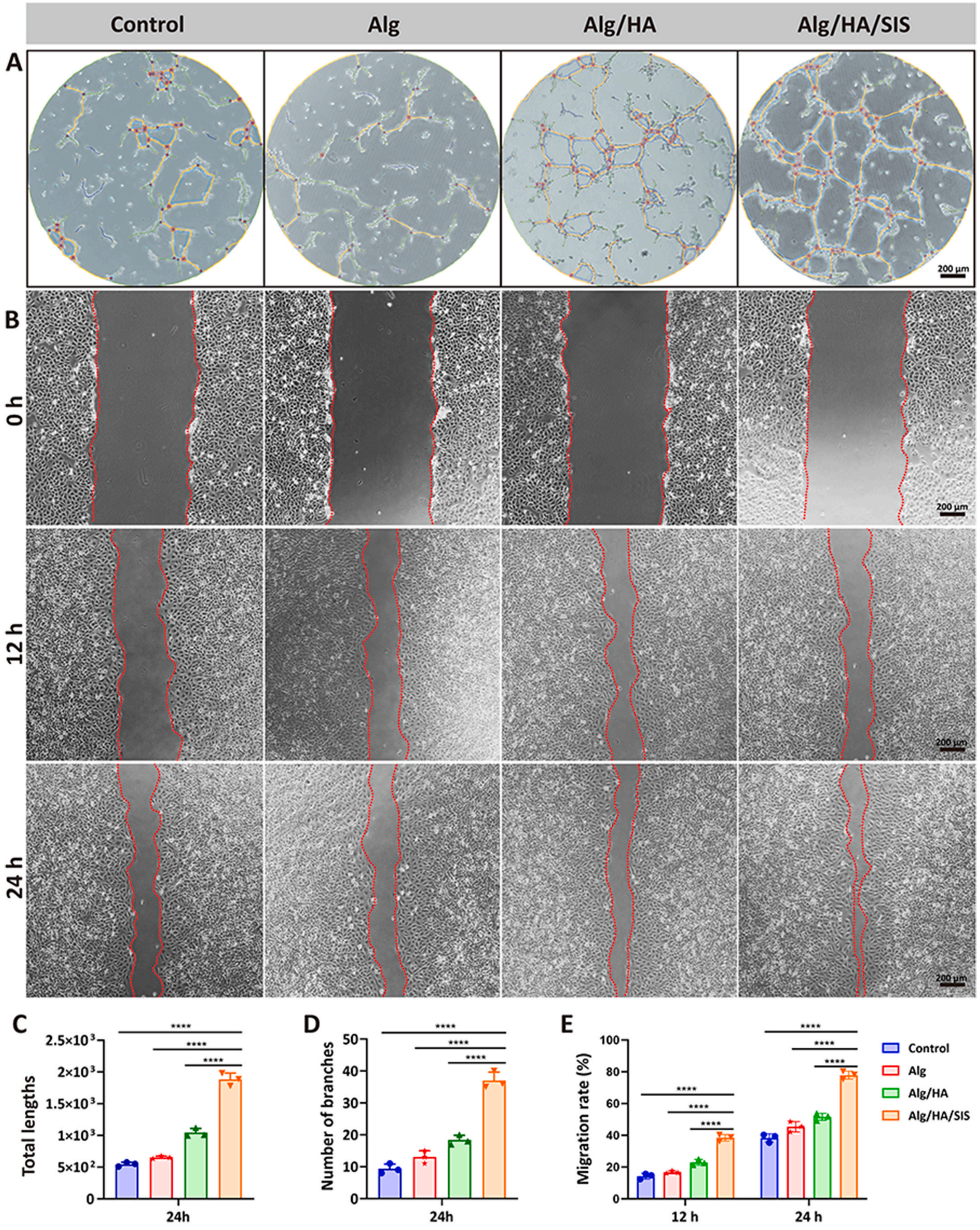

Fig. 4. *In vitro* angiogenic performances of different 3D-printed scaffolds. (A) Tube formation assay; (B) Migration of HUVECs; (C–E) Histogram of total lengths (C), number of branches (D) and migration rate (E). 3 replicates were repeated in each groups. ****$p < 0.001$.

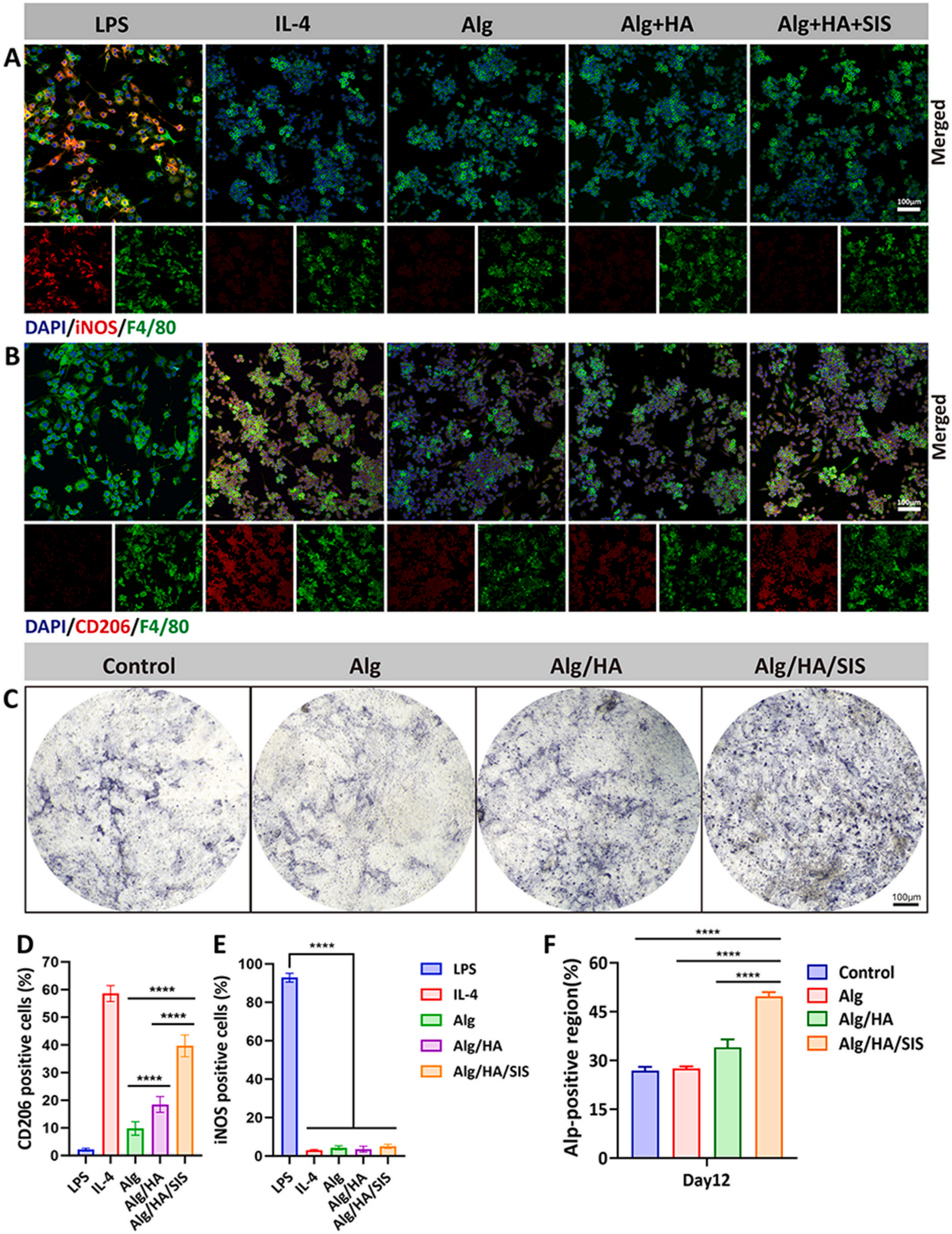

Fig. 5. *In vitro* responses of macrophages to different 3D-printed scaffolds. (A) Immunofluorescent staining of M1 marker (iNOS); (B) Immunofluorescent staining of M2 marker (CD206); (C) ALP staining; (E) Statistical histogram of the iNOS staining result; (D) Statistical histogram of the CD206 staining result; (F) Statistical histogram of the ALP staining result. 3 replicates were repeated in each groups. $^{****}p < 0.0001$.

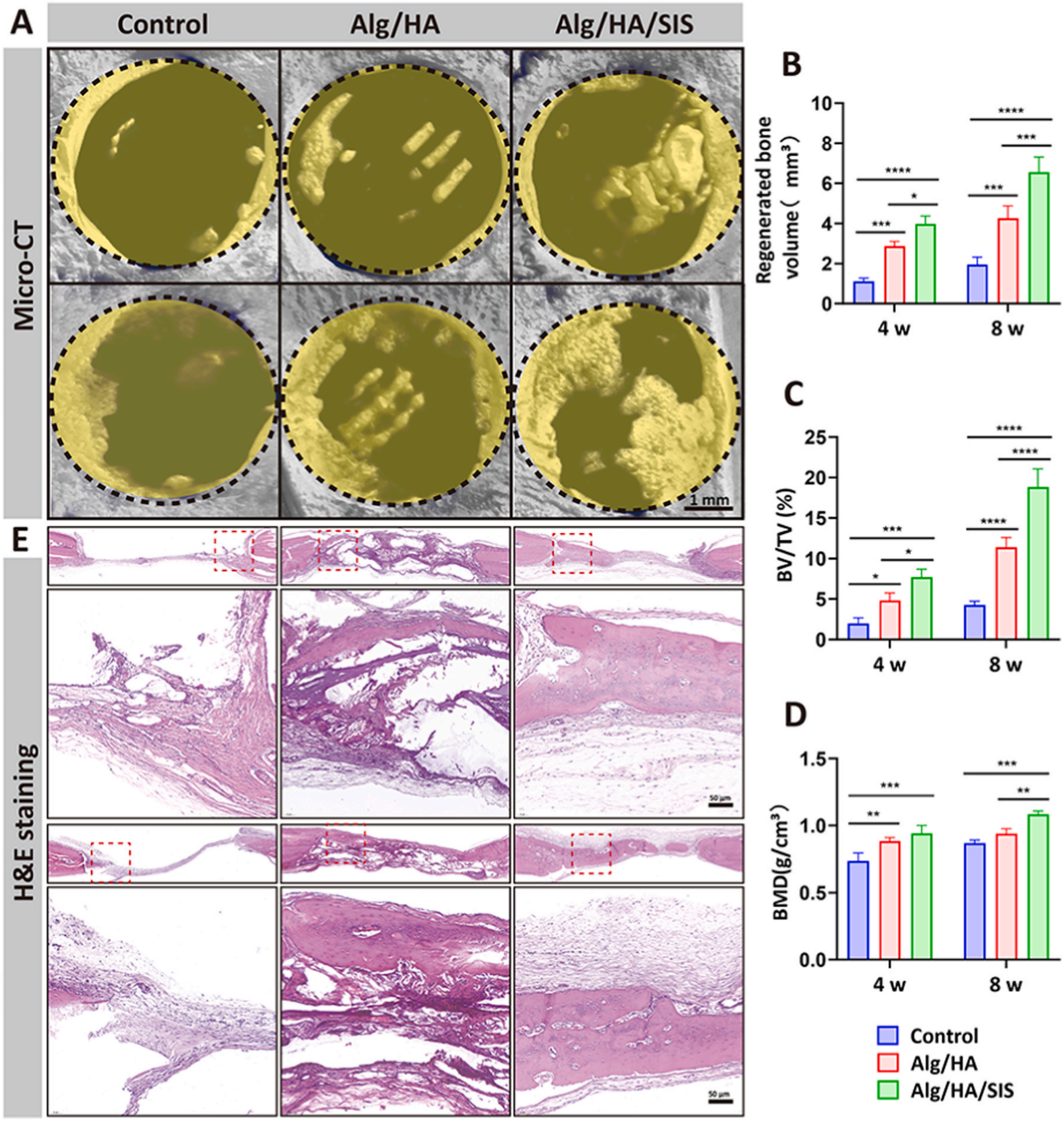

Fig. 6. *In vitro* osteogenic performances of different 3D-printed scaffolds. (A) Micro-CT scanning; (B–D) Statistical histograms of regenerated bone volume (B), BV/TV (C), and BMD (D) based on micro-CT scanning; (E) HE staining. 3 replicates were repeated in each groups. *$p < 0.05$, **$p < 0.01$, ***$p < 0.001$, ****$p < 0.0001$.

control group), although the differences between the Alg/HA group and the control group were not as strong as that between the Alg/HA/SIS group and the control group. Hence, the incorporation of bioactive compounds such as SIS is desirable for diabetic bone repair [34].

3.9. Immunohistochemical and immunofluorescent analysis: elevated ALP, CD206 and CD31 were responsible for the acceleration of bone healing in diabetic rats

As currently reported, ALP was regarded as a marker of early-stage osteogenesis. In this study, the immunohistochemical staining of ALP was investigated to explore the *in vivo* osteogenic property of the 3D-printed scaffold. The results of ALP revealed that the highest expression was observed in the Alg/HA/SIS group after 4 weeks of implantation (18.87 ± 0.94 %, $p < 0.05$, *vs.* the control and Alg/HA groups), with stronger ALP expressions detected at the peripheral interface of the implanted scaffolds (Fig. 7D and E). However, the expressions of ALP slightly declined as the regenerative process proceeded among all groups, where the elevation of late-stage osteogenic markers such as OCN and OPN would be followed [47]. Despite this decline, the highest expression of ALP was constantly observed in the Alg/HA/SIS group at both time points, which aligned with the trend of micro-CT analyses.

According to previous studies, the disruption of early-stage immune response and followed reduction of small blood vessels are responsible for the non-healing diseases associated with diabetes. In this study, the *in vivo* immunomodulatory and angiogenic effects of those 3D-printed scaffolds was evaluated by assessing the immunofluorescences of CD206 and CD31. As shown in Fig. 8A and C, the expressions of CD206 were gradually elevated post-implantation, with the strongest expressions detected in the Alg/HA/SIS group either after 3 or 7 days ($p < 0.05$, *vs.* the control and Alg/HA groups), in line with the findings that observed *in vitro*. Similarly, the highest expression of CD31 (a typical biomarker of angiogenesis) was observed in the Alg/HA/SIS group after 7 and 14 days of implantation (Fig. 8B–D). Furthermore, the diameter of newly formed vessels was gradually increased post-implantation, while still with the largest vessel diameter (16.31 ± 3.95 μm) being observed

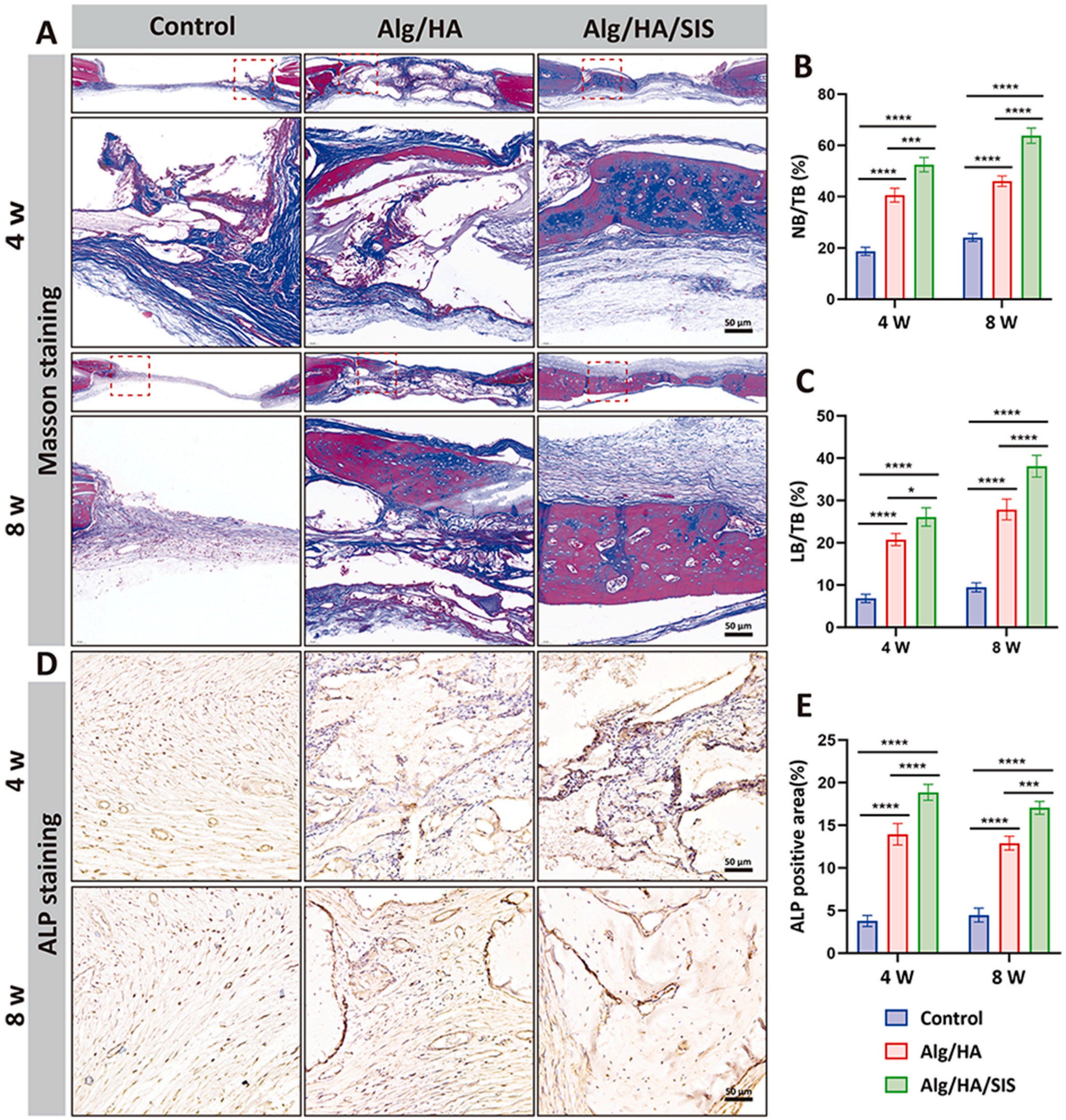

Fig. 7. *In vivo* osteogenic performances of different 3D-printed scaffolds under diabetic condition. (A) Masson staining; (B–C) Statistical histograms of NB/TB (B) and LB/TB (C) based on Masson scanning; (D) Immunohistochemical staining of ALP; (E) Statistical histogram of ALP staining. 3 replicates were repeated in each groups. $*p < 0.05$, $**p < 0.01$, $***p < 0.001$, $****p < 0.0001$.

in the Alg/HA/SIS group (Fig. 8E). Clearly, the *in vivo* immunomodulatory and angiogenic performances of Alg/HA/SIS group were superior to those of the control and Alg/HA scaffolds, which significantly facilitate the healing process under diabetic condition, in line with previously published study [48].

4. Conclusion

Disturbances in the immune response and the reduction of small blood vessels have been identified as contributing factors that impede the healing process of diabetic bone disease. Previous studies have demonstrated that SIS possesses favorable immunomodulatory and angiogenic properties, whose properties align well with the functional requirements for treating diabetic bone defects. However, the weak mechanical and gelling properties of SIS are far from satisfactory for the construction of bone scaffold *via* 3D printing. To address those issues, a novel approach by combining alginate acid, nano-hydroxyapatite, and SIS was employed to fabricate a 3D-printed composite scaffold.

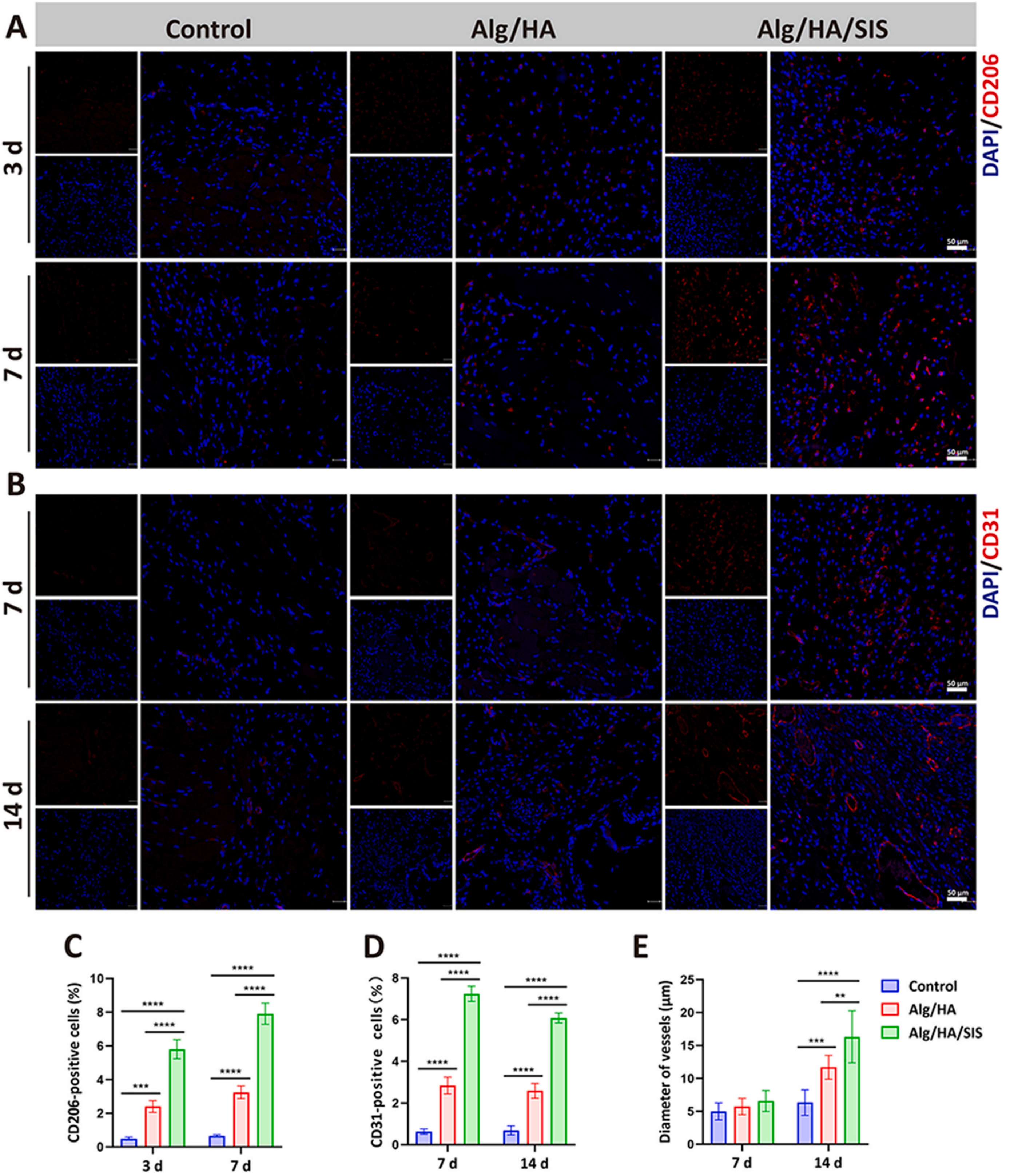

Fig. 8. *In vivo* immunomodulatory and angiogenic performances of those 3D-printed scaffolds under diabetic condition. (A) Immunofluorescent staining of M2 marker (CD206); (B) Immunofluorescent staining of angiogenic maker (CD31); (C) Statistical histogram of the CD206 staining result; (D) Statistical histogram of the CD31 staining result; (E) Statistical histogram of the diameter of newly formed blood vessels. 6 replicates were repeated in each groups. $^{**}p < 0.01$, $^{***}p < 0.001$, $^{****}p < 0.0001$.

Followed studies showed that the fabricated 3D-printed Alg/HA/SIS composite scaffold provided not only desirable immunomodulatory effect, but also good osteogenic and angiogenic performances *in vitro* and *in vivo*, which properties well-matched with the requirement for treating diabetic bone defects.

Data availability

Data will be provided by the corresponding author at reasonable request.

CRediT authorship contribution statement

Jie Tan: Formal analysis, Methodology, Writing – original draft. **Zecai Chen:** Methodology, Formal analysis, Statistics, Writing – original draft. **Zhen Xu:** Formal analysis, Methodology. **Yafang Huang:** Histology. Jun Chen, Methodology. **Lei Qin:** Methodology. **Yufeng Long:** Methodology. **Jiayi Wu:** Methodology. **Wanrong Luo:** Methodology. **Xuchao Liu:** Methodology. **Weihong Yi:** Methodology, Conceptualization. **Huaiyu Wang:** Methodology, Research supervision, Draft revision. **Dazhi Yang:** Methodology, Research supervision, Draft revision.

Declaration of AI and AI-assisted technologies in the writing process

The authors declare that no AI and AI-assisted technologies are used, and the languages in this study are manually polished by a specialist who has studied and worked in English-speaking country for many years.

Declaration of competing interest

The authors declare that they have no known competing financial interests or personal relationships that could have appeared to influence the work reported in this paper.

Acknowledgement

This study has been jointly sponsored by Guangdong Basic and Applied Basic Research Foundation of Guangdong Province-Zhongwei Biological Research Transformation Center Joint Program (Grant No. 2022A1515220036 and 2023A1515220194), Shenzhen Science and Technology Program (JSGG20210802153156021), and Major Project of Nanshan Health Committee (Grant No. NSZD2023036, NSZD2023009, NSZD2024019, and NS2024011), Nanshan District, Shenzhen, and Project of Nanshan People's Hospital (Grant No. YN2022010).

Appendix A. Supplementary data

Supplementary data related to this article can be found at https://doi.org/10.1016/j.jot.2024.07.006.

References

[1] Chen Y, Gan W, Cheng Z, Zhang A, Shi P, Zhang Y. Plant molecules reinforce bone repair: novel insights into phenol-modified bone tissue engineering scaffolds for the treatment of bone defects. Mater Today Bio 2024;24:100920.
[2] Wang Z, Geest ICV, Leeuwenburgh SC, van den Beucken JJ. Bifunctional bone substitute materials for bone defect treatment after bone tumor resection. Mater Today Bio 2023;23:100889.
[3] Wu Z, Bai J, Ge G, Wang T, Feng S, Ma Q, et al. Regulating macrophage polarization in high glucose microenvironment using lithium-modified bioglass-hydrogel for diabetic bone regeneration. Adv Healthcare Mater 2022;11(13):e2200298.
[4] Tian Y, Cui Y, Ren G, Fan Y, Dou M, Li S, et al. Dual-functional thermosensitive hydrogel for reducing infection and enhancing bone regeneration in infected bone defects. Mater Today Bio 2024;25:100972.
[5] Kang Y, Xu J, Meng L, Su Y, Fang H, Liu J, et al. 3D bioprinting of dECM/Gel/QCS/nHAp hybrid scaffolds laden with mesenchymal stem cell-derived exosomes to improve angiogenesis and osteogenesis. Biofabrication 2023;15(2):024103.
[6] Wang S, Gu R, Wang F, Zhao X, Yang F, Xu Y, et al. 3D-Printed PCL/Zn scaffolds for bone regeneration with a dose-dependent effect on osteogenesis and osteoclastogenesis. Mater Today Bio 2022;13:100202.
[7] Xu Z, Qi X, Bao M, Zhou T, Shi J, Xu Z, et al. Biomineralization inspired 3D printed bioactive glass nanocomposite scaffolds orchestrate diabetic bone regeneration by remodeling micromilieu. Bioact Mater 2023;25:239–55.
[8] Wang P, Rui H, Gao C, Wen C, Pan H, Liu W, et al. Bioprinting living organs: the next milestone in organ transplantation? The Innovation Life 2023;1(2):100019.
[9] Wong SL, Demers M, Martinod K, Gallant M, Wang Y, Goldfine AB, et al. Diabetes primes neutrophils to undergo NETosis, which impairs wound healing. Nat Med 2015;21(7):815–9.
[10] Sheu A, Greenfield JR, White CP, Center JR. Contributors to impaired bone health in type 2 diabetes. Trends Endocrinol Metabol 2023;34(1):34–48.
[11] Mariadoss AVA, Sivakumar AS, Lee CH, Kim SJ. Diabetes mellitus and diabetic foot ulcer: etiology, biochemical and molecular based treatment strategies via gene and nanotherapy. Biomed Pharmacother 2022;151:113134.
[12] Hygum K, Starup-Linde J, Harsløf T, Vestergaard P, Langdahl BL. Mechanisms in endocrinology: diabetes mellitus, a state of low bone turnover - a systematic review and meta-analysis. Eur J Endocrinol 2017;176(3):R137–9.
[13] Khosla S, Samakkarnthai P, Monroe DG, Farr JN. Update on the pathogenesis and treatment of skeletal fragility in type 2 diabetes mellitus. Nat Rev Endocrinol 2021;17(11):685–97.
[14] Lecka-Czernik B. Diabetes, bone and glucose-lowering agents: basic biology. Diabetologia 2017;60(7):1163–9.
[15] Le T, Salas Sanchez A, Nashawi D, Kulkarni S, Prisby RD. Diabetes and the microvasculature of the bone and marrow. Curr Osteoporos Rep 2024;22(1):11–27.
[16] Wang X, Lin M, Kang Y. Engineering porous β-tricalcium phosphate (β-TCP) scaffolds with multiple channels to promote cell migration, proliferation, and angiogenesis. ACS Appl Mater Interfaces 2019;11(9):9223–32.
[17] Li Q, Li Q, Lu S, Pan D. Spatial topological structure design of porous Ti-6Al-4V alloy with low modulus and magnetic susceptibility. Nanomaterials 2023;13(24):3113.
[18] Yang SY, Zhou YN, Yu XG, Fu ZY, Zhao CC, Hu Y, et al. A xonotlite nanofiber bioactive 3D-printed hydrogel scaffold based on osteo-/angiogenesis and osteoimmune microenvironment remodeling accelerates vascularized bone regeneration. J Nanobiotechnol 2024;22(1):59.
[19] Wang X, Liu A, Zhang Z, Hao D, Liang Y, Dai J, et al. Additively manufactured Zn-2Mg alloy porous scaffolds with customizable biodegradable performance and enhanced osteogenic ability. Adv Sci 2024;11(5):e2307329.
[20] Xie L, Wang G, Wu Y, Liao Q, Mo S, Ren X, et al. Programmed surface on poly(aryl-ether-ether-ketone) initiating immune mediation and fulfilling bone regeneration sequentially. Innovation 2021;2(3):100148.
[21] Yang T, Dong Y, Wan J, Liu X, Liu Y, Huang J, et al. Sustained release of BMSC-EVs from 3D printing gel/HA/nHAP scaffolds for promoting bone regeneration in diabetic rats. Adv Healthcare Mater 2023;12(18):e2203131.
[22] Chen S, Cheng D, Bao W, Ding R, Shen Z, Huang W, et al. Polydopamine-functionalized strontium alginate/hydroxyapatite composite microhydrogel loaded with vascular endothelial growth factor promotes bone formation and angiogenesis. ACS Appl Mater Interfaces 2024;16(4):4462–77.
[23] Sheng N, Xing F, Wang J, Zhang QY, Nie R, Li-Ling J, et al. Recent progress in bone-repair strategies in diabetic conditions. Mater Today Bio 2023;23:100835.
[24] Wu Y, Wang H, Chu PK. Enhancing macrophages to combat intracellular bacteria. The Innovation Life 2023;1(2):100027.
[25] Wang W, Zhang X, Chao N-N, Qin T-W, Ding W, Zhang Y, et al. Preparation and characterization of pro-angiogenic gel derived from small intestinal submucosa. Acta Biomater 2016;29:135–48.
[26] Zhang Q-Y, Tan J, Nie R, Song Y-T, Zhou X-L, Feng Z-Y, et al. Acceleration of wound healing by composite small intestinal submucosa hydrogels through immunomodulation. Compos B Eng 2023;254:110550.
[27] Zhang X-Z, Jiang Y-L, Hu J-G, Zhao L-M, Chen Q-Z, Liang Y, et al. Procyanidins-crosslinked small intestine submucosa: a bladder patch promotes smooth muscle regeneration and bladder function restoration in a rabbit model. Bioact Mater 2021;6(6):1827–38.
[28] Tan J, Zhang Q-Y, Song Y-T, Huang K, Jiang Y-L, Chen J, et al. Accelerated bone defect regeneration through sequential activation of the M1 and M2 phenotypes of macrophages by a composite BMP-2@SIS hydrogel: an immunomodulatory perspective. Compos B Eng 2022;243:110149.
[29] Nie R, Zhang Q-Y, Tan J, Feng Z-Y, Huang K, Sheng N, et al. EGCG modified small intestine submucosa promotes wound healing through immunomodulation. Compos B Eng 2023;267:111005.
[30] Sheng N, Xing F, Zhang Q-Y, Tan J, Nie R, Huang K, et al. A pleiotropic SIS-based hydrogel with immunomodulation via NLRP3 inflammasome inhibition for diabetic bone regeneration. Chem Eng J 2024;480:147985.
[31] Tan J, Zhang QY, Huang LP, Huang K, Xie HQ. Decellularized scaffold and its elicited immune response towards the host: the underlying mechanism and means of immunomodulatory modification. Biomater Sci 2021;9(14):4803–20.
[32] Li J, Han J, Yu W, Wang K, Liu Z, Liu Y. Alginate-modulated continuous assembly of iron/tannic acid composites as photothermally responsive wound dressings for hemostasis and drug resistant bacteria eradication. Int J Biol Macromol 2023;242(Pt 2):124886.
[33] Wang H, Yang J, Tian W, Peng K, Xue Y, Zhao H, et al. A sodium alginate/carboxymethyl chitosan dual-crosslinked injectable hydrogel scaffold with tunable

softness/hardness for bone regeneration. Int J Biol Macromol 2024;257(Pt 2):128700.

[34] Lee J, Hong J, Kim W, Kim GH. Bone-derived dECM/alginate bioink for fabricating a 3D cell-laden mesh structure for bone tissue engineering. Carbohydr Polym 2020;250:116914.

[35] Akshata CR, Murugan E, Harichandran G. Alginate templated synthesis, characterization and in vitro osteogenic evaluation of strontium-substituted hydroxyapatite. Int J Biol Macromol 2023;252:126478.

[36] Wang Y, Wang X, Liu X, Niu C, Yu G, Hou Y, et al. Fabrication, characterization and potential application of biodegradable polydopamine-modified scaffolds based on natural macromolecules. Int J Biol Macromol 2023;253(Pt 1):126596.

[37] de Melo Pereira D, Davison N, Habibović P. Human osteoclast formation and resorptive function on biomineralized collagen. Bioact Mater 2022;8:241–52.

[38] Ghosh S, Pati F. Decellularized extracellular matrix and silk fibroin-based hybrid biomaterials: a comprehensive review on fabrication techniques and tissue-specific applications. Int J Biol Macromol 2023;253(Pt 8):127410.

[39] Donate R, Paz R, Quintana Á, Bordón P, Monzón M. Calcium carbonate coating of 3D-printed PLA scaffolds intended for biomedical applications. Polymers 2023;15(11):2506.

[40] Sadeghian A, Kharaziha M, Khoroushi M. Dentin extracellular matrix loaded bioactive glass/GelMA support rapid bone mineralization for potential pulp regeneration. Int J Biol Macromol 2023;234:123771.

[41] Azaryan E, Mortazavi-Derazkola S, Alemzadeh E, Emadian Razavi F, Yousefi M, Hanafi-Bojd MY, et al. Effects of hydroxyapatite nanorods prepared through Elaeagnus Angustifolia extract on modulating immunomodulatory/dentin-pulp regeneration genes in DPSCs. Odontology 2023;111(2):461–73.

[42] Al-Hamoudi F, Rehman HU, Almoshawah YA, Talari ACS, Chaudhry AA, Reilly GC, et al. Bioactive composite for orbital floor repair and regeneration. Int J Mol Sci 2022;23(18).

[43] Lazarevic M, Petrovic S, Pierfelice TV, Ignjatovic N, Piattelli A, Vlajic Tovilovic T, et al. Antimicrobial and osteogenic effects of collagen membrane decorated with chitosan-nano-hydroxyapatite. Biomolecules 2023;13(4):10333.

[44] Zhang J, Tong D, Song H, Ruan R, Sun Y, Lin Y, et al. Osteoimmunity-regulating biomimetically hierarchical scaffold for augmented bone regeneration. Adv Mater 2022;34(36):e2202044.

[45] Li J, Song J, Meng D, Yi Y, Zhang T, Shu Y, et al. Electrospun naringin-loaded microsphere/sucrose acetate isobutyrate system promotes macrophage polarization toward M2 and facilitates osteoporotic bone defect repair. Regen Biomater 2023;10:rbad006.

[46] Gurucharan I, Saravana Karthikeyan B, Mahalaxmi S, Baskar K, Rajkumar G, Dhivya V, et al. Characterization of nano-hydroxyapatite incorporated carboxymethyl chitosan composite on human dental pulp stem cells. Int Endod J 2023;56(4):486–501.

[47] Wang Y, Xia C, Chen Y, Jiang T, Hu Y, Gao Y. Resveratrol synergistically promotes BMP9-induced osteogenic differentiation of mesenchymal stem cells. Stem Cell Int 2022;2022:1–13.

[48] Suh JW, Lee KM, Ko EA, Yoon DS, Park KH, Kim HS, et al. Promoting angiogenesis and diabetic wound healing through delivery of protein transduction domain-BMP2 formulated nanoparticles with hydrogel. J Tissue Eng 2023;14:1–16.